A proposal for highly tunable optical parametric oscillation in silicon micro-resonators

Q. Lin, T. J. Johnson, R. Perahia, C. P. Michael, and O. J. Painter

Department of Applied Physics, California Institute of Technology, Pasadena, CA 91125

linq@caltech.edu

Abstract: We propose a novel scheme for continuous-wave pumped optical parametric oscillation (OPO) inside silicon micro-resonators. The proposed scheme not only requires a relative low lasing threshold, but also exhibits extremely broad tunability extending from the telecom band to mid infrared.

© 2008 Optical Society of America

OCIS codes: (190.4390) Nonlinear optics, integrated optics; (130.3990) Micro-optical devices; (190.4380) Four-wave mixing; (190.4970) Parametric oscillators and amplifiers.

References and links

1. R. Soref, "The Past, Present, and Future of Silicon Photonics," IEEE J. Sel. Top. Quantum Electron. **12**, 1678–1687 (2006), and references therein.
2. Q. Lin, O. J. Painter, and G. P. Agrawal, "Nonlinear optical phenomena in silicon waveguides: Modeling and applications," Opt. Express **15**, 16604–16644 (2007).
3. V. Raghunathan, R. Claps, D. Dimitropoulos, and B. Jalali, "Parametric Raman wavelength conversion in scaled silicon waveguides," J. Lightwave Technol. **23**, 2094–2102 (2005).
4. H. Fukuda, K. Yamada, T. Shoji, M. Takahashi, T. Tsuchizawa, T. Watanabe, J. Takahashi, and S. Itabashi, "Four-wave mixing in silicon wire waveguides," Opt. Express **13**, 4629–4637 (2005).
5. H. Rong, Y. Kuo, A. Liu, M. Paniccia, and O. Cohen, "High efficiency wavelength conversion of 10 Gb/s data in silicon waveguides," Opt. Express **14**, 1182–1188 (2006).
6. M. A. Foster, A. C. Turner, R. Salem, M. Lipson, and A. L. Gaeta, "Broad-band continuous-wave parametric wavelength conversion in silicon nanowaveguides," Opt. Express **15**, 12949–12958 (2007).
7. I-W. Hsieh, X. Chen, J. I. Dadap, N. C. Panoiu, R. M. Osgood, Jr., S. J. McNab, and Y. A. Vlasov, "Cross-phase modulation-induced spectral and temporal effects on co-propagating femtosecond pulses in silicon photonic wires," Opt. Express **15**, 1135–1146 (2007).
8. A. C. Turner, M. A. Foster, A. L. Gaeta, and M. Lipson, "Ultra-low power parametric frequency conversion in a silicon microring resonator," Opt. Express **16**, 4881-4887 (2008).
9. Q. Lin, J. Zhang, P. M. Fauchet, and G. P. Agrawal, "Ultrabroadband parametric generation and wavelength conversion in silicon waveguides," Opt. Express **14**, 4786–4799 (2006).
10. M. Dinu, F. Quochi, and H. Garcia, "Third-order nonlinearities in silicon at telecom wavelengths," Appl. Phys. Lett. **82**, 2954–2956 (2003).
11. A. D. Bristow, N. Rotenberg, and H. M. van Driel, "Two-photon absorption and Kerr coefficients of silicon for 850-2200 nm," Appl. Phys. Lett. **90**, 191104 (2007).
12. Q. Lin, J. Zhang, G. Piredda, R. W. Boyd, P. M. Fauchet, and G. P. Agrawal, "Dispersion of silicon nonlinearities in the near-infrared region," Appl. Phys. Lett. **90**, 021111 (2007).
13. G. P. Agrawal, *Nonlinear Fiber Optics*, 4th ed. (Academic Press, Boston, 2007).
14. Although the waveguide shown in Fig. 1 is multimoded over a broad spectral range, higher-order modes have quite different mode profiles and dispersion properties compared with the fundamental quasi-TE mode. They are not likely to participate in the FWM process if the pump and signal waves propagate predominantly in the fundamental quasi-TE mode.
15. The real and imaginary parts of $\chi^{(3)}$ are related to Kerr nonlinearity and TPA, respectively [2]. An accurate description of SPM, XPM, TPA, and FWM requires complete information about $\chi^{(3)}(-\omega_i;\omega_j,-\omega_k,\omega_l)$. However, current experimental knowledge is only available for $\chi^{(3)}(-\omega_i;\omega_i,-\omega_i,\omega_i)$ [11, 12]. As cross-TPA involves the simultaneous absorption of two photons at ω_i and ω_j, we approximate $\chi^{(3)}(-\omega_i;\omega_j,-\omega_j,\omega_i) \approx$

$\chi^{(3)}(-\bar{\omega};\bar{\omega},-\bar{\omega},\bar{\omega})$ where $\bar{\omega}=(\omega_i+\omega_j)/2$. Similarly, FWM involves the annihilation of two pump photons to create a signal and idler photon, and we approximate $\chi^{(3)}(-\omega_s;\omega_p,-\omega_i,\omega_p)\approx\chi^{(3)}(-\omega_p;\omega_p,-\omega_p,\omega_p)$. Note also $\chi^{(3)}(-\omega_i;\omega_p,-\omega_s,\omega_p)=\chi^{(3)}(-\omega_s;\omega_p,-\omega_i,\omega_p)=[\chi^{(3)}(-\omega_p;\omega_s,-\omega_p,\omega_i)]^*$ because of the time-reversal symmetry.

16. We fit each set of experimental data ($1.2-2.2$ μm) in Refs. [11, 12] with a fifth-order polynomial, and average them to obtain the silicon nonlinearity. TPA is zero and the Kerr nonlinearity is assumed to be constant for wavelength longer than 2.2 μm.

17. R. A. Soref and B. R. Bennett, "Electrooptical effects in silicon," IEEE J. Quantum Electron. **23**, 123–129 (1987).

18. For completeness, we have included all possible self- and cross-TPA and induced free carriers from all the three waves and their combinations in the numerical results of this paper.

19. A. Y. H. Chen, G. K. L. Wong, S. G. Murdoch, R. Leonhardt, J. D. Harvey, J. C. Knight, W. J. Wadsworth, and P. St. J. Russell, "Widely tunable optical parametric generation in a photonic crystal fiber," Opt. Lett. **30**, 762–764 (2005).

20. Y. Deng, Q. Lin, F. Lu, G. P. Agrawal, and W. H. Knox, "Broadly tunable femtosecond parametric oscillator using a photonic crystal fiber," Opt. Lett. **30**, 1234–1236 (2005).

21. T. V. Andersen, K. M. Hilligsøe, C. K. Nielsen, J. Thøgersen, K. P. Hansen, S. R. Keiding, and J. J. Larsen, "Continuous-wave wavelength conversion in a photonic crystal fiber with two zero-dispersion wavelengths," Opt. Express **12**, 4113-4122 (2004).

22. M. Borselli, T. J. Johnson, and O. J. Painter, "Beyond the Rayleigh scattering limit in high-Q silicon microdisks: theory and experiment", Opt. Express **13**, 1515–1529 (2005).

23. T. J. Kippenberg, S.M. Spillane, and K. J. Vahala, "Kerr-Nonlinearity Optical Parametric Oscillation in an Ultrahigh-Q Toroid Microcavity," Phys. Rev. Lett. **93**, 083904 (2004).

24. C. P. Michael, M. Borselli, T. J. Johnson, C. Chrystal, and O. Painter, "An optical fiber-taper probe for wafer-scale microphotonic device characterization," Opt. Express **15**, 4745–4752 (2007).

25. In practice, a critical coupling over such a broad spectral region is difficult for a straight bus waveguide, but is possible by using a curved bus waveguide with a curvature similar to the resonator. See T. Carmon, S. Y. T. Wang, E. P. Ostby, and K. J. Vahala, "Wavelength-independent coupler from fiber to an on-chip cavity, demonstrated over an 850nm span," Opt. Express **15**, 7677–7681 (2007).

26. I. T. Sorokina and K. L. Vodopyanov, Eds., *Solid-State Mid-Infrared Laser Sources*, Top. Appl. Phys. **89** (2003).

27. B. Jalali, V. Raghunathan, R. Shori, S. Fathpour, D. Dimitropoulos, and O. Strafsudd, "Propests for silicon mid-IR Raman lasers," IEEE J. Sel. Top. Quantum Electron. **12**, 1618–1627 (2006).

28. M. Krause, R. Draheim, H. Renner, and E. Brinkmeyer, "Cascaded silicon Raman lasers as mid-infrared sources," IEE Electron. Lett. **42**, 1224–1225 (2006).

29. H. Rong, S. Xu, O. Cohen, O. Raday, M. Lee, V. Sih, and M. Paniccia, "A cascaded silicon Raman laser," Nature Photon. **2**, 170 (2008).

30. P. E. Barclay, K. Srinivasan, and O. Painter, "Nonlinear response of silicon photonic crystal microresonators excited via an integrated waveguide and fiber taper," Opt. Express **13**, 801-820 (2005).

1. Introduction

Silicon photonics has attracted much attention recently because of its great application potential in the broad near and mid infrared spectral regions [1]. In particular, silicon exhibits a significant third-order nonlinearity. This feature, together with the tight mode confinement provided by silicon-on-insulator (SOI) waveguides, makes it possible to realize a variety of optical functions on a submicron scale at relatively low power levels [1]– [8]. However, intense optical waves inside the waveguides/microresonators also introduce two-photon absorption (TPA) which generates a significant number of free carriers. These free carriers impose a severe absorption background and become the major obstacle to the practical implementation of silicon nonlinear devices. In this paper, we propose a novel scheme to realize a light source on the SOI platform through four-wave mixing (FWM), which is not only free from the severe free-carrier absorption (FCA), but also provides extremely large tunability extending from the telecom band to the mid infrared. We provide detailed theoretical analysis to show the high efficiency of the proposed scheme for parametric amplification and the low threshold requirement for parametric oscillation by applying such scheme inside a micro-resonator.
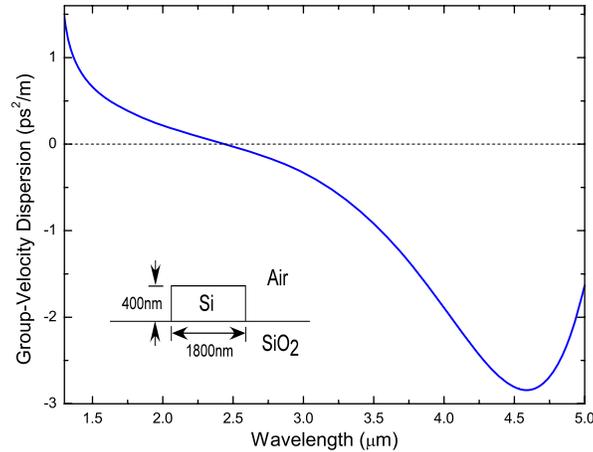
Fig. 1. Group velocity dispersion for a straight waveguide with a geometry shown in the inset, simulated by the finite element method (FEMLAB, COMSOL).

2. Optical parametric amplification

We focus on the degenerate FWM configuration in which a single continous-wave (CW) pump is employed. FWM occurs through $2\omega_p = \omega_s + \omega_i$, where ω_j ($j = p,s,i$) are the frequencies for the pump, signal, and idler waves, respectively. FWM in silicon occurs through a nonresonant electronic response. It is nearly instantaneous and thus enables parametric generation to exist over a broad bandwidth [2,9]. Although FCA limits FWM to a low efficiency in the telecom band [3]– [9], TPA vanishes for the pump wave when its frequency is tuned below the half band gap at $E_g/2 = 0.56$ eV (corresponding to a photon wavelength of around 2.2 μm) [11, 12], leading to a negligible population of free carriers and thus enabling efficient parametric generation.

Moreover, FWM is a coherent process and requires phase matching among the interacting waves. It turns out that the phase matching condition is very sensitive to the group-velocity dispersion (GVD) of the waveguide/resonator [13]. In general, quasi-phase matching can be satisfied over a broad band if the pump wavelength is located in the vicinity of zero-dispersion wavelength (ZDWL). Therefore, by appropriately designing the waveguide geometry to tailor the ZDWL below the half band gap where the pump is located, it is possible to satisfy the phase matching condition at wavelengths far from the pump and thus create signal waves well above the half band gap. Figure 1 shows such an example. For a waveguide dimension of 1.8×0.4 μm, the ZDWL of the fundamental quasi-TE mode can be tailored to around 2439 nm, beyond which GVD becomes anomalous. In the following, we will show that highly tunable parametric oscillation can be realized inside a resonator with such kind of waveguide geometry.

To simplify the analysis, we focus on the case where the three waves are identically polarized in the fundamental quasi-TE mode inside a waveguide fabricated along the [0 1 0] crystallo-graphic axis on a (1 0 0) wafer [14]. As the nonlinear effects in this mode are dominated by its transverse polarization component (its longitudinal component along the propagation z direction contains only a small fraction of incident power), we can simplify the problem con-siderably by adopting a scalar approach. The pump, signal, and idler waves are found to satisfy the following equations [2,9]:

$$\frac{\partial A_p}{\partial z} = \left\{ i(\beta_p + \beta_p^{\mathrm{f}}) - \alpha_{\mathrm{lp}}/2 \right\} A_p + i \left(\gamma_{\mathrm{p}} P_p + 2\gamma_{\mathrm{ps}} P_s + 2\gamma_{\mathrm{pi}} P_i \right) A_p + 2i\gamma_{\mathrm{pspi}} A_s A_i A_p^*, \qquad (1)$$

$$\frac{\partial A_s}{\partial z} = \left\{i(\beta_s + \beta_s^{\mathrm{f}}) - \alpha_{\mathrm{ls}}/2\right\}A_s + i\left(\gamma_s P_s + 2\gamma_{\mathrm{sp}}P_p + 2\gamma_{\mathrm{si}}P_i\right)A_s + i\gamma_{\mathrm{spip}}A_p^2 A_i^*, \tag{2}$$

$$\frac{\partial A_i}{\partial z} = \left\{i(\beta_i + \beta_i^{\mathrm{f}}) - \alpha_{\mathrm{li}}/2\right\}A_i + i\left(\gamma_i P_i + 2\gamma_{\mathrm{ip}}P_p + 2\gamma_{\mathrm{is}}P_s\right)A_i + i\gamma_{\mathrm{ipsp}}A_p^2 A_s^*, \tag{3}$$

where α_{lj} and β_j ($j = p,s,i$) are linear scattering loss and the propagation constant at ω_p, ω_s, and ω_i, respectively. The field amplitude A_j is normalized such that $P_j = |A_j|^2$ represents the optical power.

In the preceding equations, $\gamma_u \equiv \gamma_{\mathrm{uuuu}}$ and $\gamma_{\mathrm{uv}} \equiv \gamma_{\mathrm{uvvu}}$ ($u,v = p,s,i$ and $u \neq v$) are the nonlinear parameters for self- and cross-phase modulation (SPM and XPM), respectively. They also include the self- and cross-TPA through their imaginary parts [2]. These nonlinear parameters together with those for FWM are given by a general form of [2]

$$\gamma_{\mathrm{ijkl}} = \frac{3\omega_i \eta_{\mathrm{ijkl}} \chi^{(3)}(-\omega_i; \omega_j, -\omega_k, \omega_l)}{4\varepsilon_0 c^2 \bar{a}_{\mathrm{ijkl}} \sqrt{n_i n_j n_k n_l}}, \tag{4}$$

where $\chi^{(3)}$ is the third-order susceptibility [15] and n_v is modal refractive index at ω_v ($v = i,j,k,l$). $\bar{a}_{\mathrm{ijkl}} \equiv (a_i a_j a_k a_l)^{1/4}$ is the effective mode area related to those of individual waves a_v ($v = i,j,k,l$), and η_{ijkl} is the mode overlap factor defined as [2]

$$\eta_{\mathrm{ijkl}} \equiv \frac{\iint F_i^* F_j F_k^* F_l \, dxdy}{\left\{\prod_{v=i,j,k,l} \iint |F_v|^4 dxdy\right\}^{1/4}}, \tag{5}$$

where F_v is the transverse mode profile at ω_v. As the signal and idler can be created quite far from the pump frequency, $\chi^{(3)}$, a_v, and η_{ijkl} could all become dispersive. In particular, silicon nonlinearity changes significantly over such a broad spectral region [10–12]. Therefore, we include the dispersions for all $\chi^{(3)}$, a_v, and η_{ijkl} in our numerical analysis [15, 16].

In Eqs. (1)-(3), $\beta_j^{\mathrm{f}} = \omega_j n_{\mathrm{fj}}/c + i\alpha_{\mathrm{fj}}/2$ represents the free-carrier-induced perturbations to the propagation constant, where the induced refractive index change $n_{\mathrm{fj}}(z,t)$ and FCA coefficient $\alpha_{\mathrm{fj}}(z,t)$ are well described by the Drude model [17]. They are given by $n_{\mathrm{fj}} = -(8.8 \times 10^{-22}N + 8.5 \times 10^{-18}N^{0.8})(\lambda_j/\lambda_{\mathrm{ref}})^2$ and $\alpha_{\mathrm{fj}} = 1.45 \times 10^{-17}(\lambda_j/\lambda_{\mathrm{ref}})^2 N$, respectively, where $\lambda_{\mathrm{ref}} = 1.55$ μm and $N(z,t)$ is the density of electron-hole pairs created through TPA. As we locate the pump well below $E_g/2$, the pump itself does not introduce TPA and free carriers primarily come from the cross-TPA by simultaneously absorbing a pump and signal/idler photon whose sum energy is above E_g. As a result, N is dominated [18] by the term $N = 2\tau_0 \beta_{\mathrm{Tps}} P_p P_s / (\bar{a}_{\mathrm{pssp}}^2 \hbar\omega_p)$, where we have assumed the signal is located at the anti-Stokes side with $\omega_s > \omega_p$. $\beta_{\mathrm{Tps}} = 2\mathrm{Im}(\gamma_{\mathrm{ps}})\bar{a}_{\mathrm{pssp}}$ is the cross-TPA coefficient and τ_0 is the effective carrier lifetime, assumed to be 1 ns in this paper. As the signal power is small in general, the generated carrier density is low. For example, even for an intense 3-W pump at 2.3 μm and a coexisting 1-mW signal at 1.6 μm, $N \approx 1.36 \times 10^{15}$ cm^{-3}, corresponding to an FCA coefficient $\alpha_f \approx 0.13$ dB/cm at 4.0 μm (0.02 dB/cm at 1.6 μm). Clearly, FCA is quite small, unless the signal becomes fairly intense. Therefore, the commonly encountered FCA is not an obstacle here, and we are able to obtain significant parametric generation.

To illustrate the efficiency of our proposed scheme, we consider first the parametric amplification inside a straight waveguide with a length of 3 cm and a cross section shown in Fig. 1. For such waveguide, the effective mode area a_v changes by about 20% (0.42 to 0.50 μm^2) when the wavelength varies from 1.5 to 5 μm. However, detailed analysis shows that the fundamental modes overlap well with each other, resulting in $|\eta_{\mathrm{ijkl}}| \approx 1$, even for such widely separated waves. The linear scattering loss is assumed to be 0.2 dB/cm, same for all three waves. The signal is assumed to be as weak as 1 μW to investigate the small-signal gain for the parametric process. Figure 2 shows the parametric gain spectra with different pump wavelengths at a
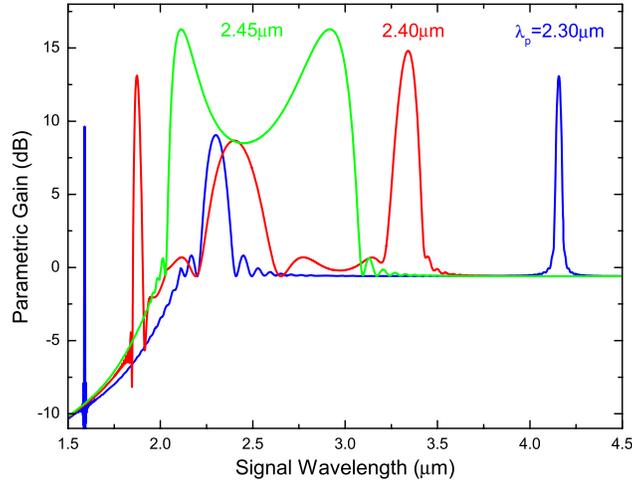
Fig. 2. Parametric gain spectra at three pump wavelengths inside a waveguide shown in Fig. 1. Parameters are given in the text.

pumping level of 3 W. The parametric gain is defined as the power ratio between the output and input signal as $G = 10\log_{10}[P_s(L)/P_s(0)]$. When the pump wavelength is located in the anomalous-dispersion regime of 2.45 μm (green curve), SPM and XPM from the pump assist the phase matching [13] to realize a broadband gain spectra from 2.04 to 3.08 μm with a peak gain of 16.3 dB. However, when the pump wavelength is tuned to a slightly normal-dispersion region at 2.40 μm (red curve), phase matching enables parametric amplification for widely separated signal and idler located around 1873 nm and 3340 nm, with peak gains of 13.1 and 14.8 dB, respectively, and a 3-dB bandwidth of 26 nm (at 1873 nm). Further tuning of the pump wavelength to 2.30 μm would dramatically shift the parametric gain peak to 1590 nm (corresponding idler at 4156 nm), as shown in the blue curve. Efficient FWM provides a peak gain of 9.6 dB with a 3-dB bandwidth of 3 nm, although otherwise cross-TPA would introduce a significant loss of ~ -9 dB.

Such a broad tunability can be seen more clearly in the phase matching condition. Equations (1)-(3) show that, in the nondepleted case with a weak signal, the phase mismatch is given by

$$\kappa = \Delta\beta + \Delta\beta^{\mathrm{f}} + 2P_p\mathrm{Re}[\gamma_{\mathrm{sp}} + \gamma_{\mathrm{ip}}^* - \gamma_{\mathrm{p}}], \qquad (6)$$

where the first term represents the linear part, $\Delta\beta = \beta_s + \beta_i - 2\beta_p$ and the final term is the nonlinear part resulting from the pump-induced SPM and XPM [13]. The second term represents free-carrier-induced phase mismatch, $\Delta\beta^{\mathrm{f}} = \mathrm{Re}(\beta_s^{\mathrm{f}} + \beta_i^{\mathrm{f}} - 2\beta_p^{\mathrm{f}})$, which is negligible because of very low carrier densities generated in our proposed scheme, as discussed previously. Efficient FWM occurs when $\kappa \approx 0$. Figure 3 shows the phase-matched signal and idler wavelengths as a function of pump wavelength at a pumping level of 3 W. When the pump is located in the anomalous-dispersion regime, the nonlinear phase mismatch compensates the linear one and thus allows the signal and idler to be generated over a broad band but close to each other [13]. In this regime, increasing the pump wavelength does not affect much the spectral location of phase-matched signal/idler, except with a decreased bandwidth because of an increased GVD magnitude [9]. In contrast, when the pump wavelength is tuned to the normal-dispersion regime, high order dispersions play a significant role in the phase matching condition [19], which enables phase matching at wavelengths far away from the pump. Such high-order-dispersion assisted phase matching is sensitive to the pump wavelength and
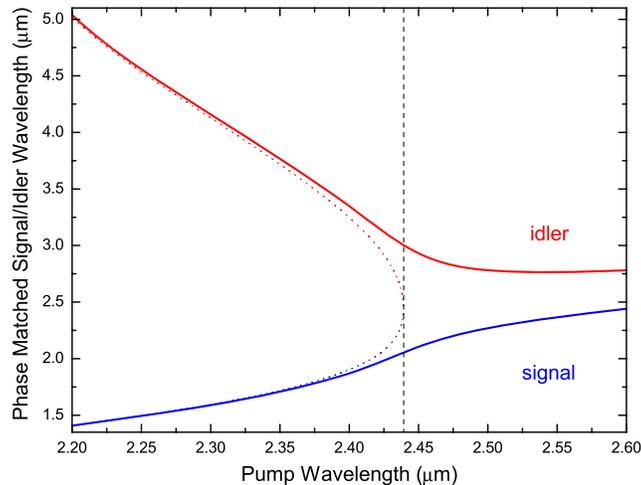
Fig. 3. Phase-matched signal and idler wavelengths as a function of pump wavelength for the waveguide geometry in Fig. 1. Solid curves show the case with a pump power of 3 W. Dotted curves shows the case of purely linear phase matching ($\Delta k = 0$) where the pump is absent. Their closeness to the solid lines in the normal-dispersion regime indicates the effect of high-order dispersion [19]. The black dashed line shows the location of the ZDWL.

thus provides broad spectral tunability of parametric gain. Figure 3 shows that tuning of pump wavelength from 2400 to 2300 nm causes the phase-matched signal to shift from 1873 to 1590 nm into the telecom band. At the same time, the idler is tuned by more than 800 nm in the mid infrared region. The spectral tunability of the signal/idler is enhanced by more than five times compared with the pump. It can be increased further by specifically designing the waveguide geometry (*i.e.*, using a photonic crystal cladding) to engineer the high-order dispersion. Equivalently, such spectral tunability can also be obtained with a fixed pump wavelength, by changing the waveguide geometry to shift the ZDWL towards longer wavelengths. As a result, the pump wavelength is not critical, as long as it is below the half band gap. Note that a similar kind of parametric generation has been observed in photonic-crystal silica fibers [19] and used to build synchronously-pumped OPO [20]. With a nonlinearity significantly larger in silicon, it is possible to realize a CW operation of OPO inside a micro-resonator with an appropriately designed waveguide geometry.

Interestingly, apart from the fundamental quasi-TE mode, the fundamental quasi-TM mode of the waveguide shown in Fig. 1 exhibits a similar ZDWL of 2354 nm [2]. However, as it is the second ZDWL of the mode with a negative third-order dispersion (its first ZDWL is around 1298 nm, see Ref. [2]), GVD shows an opposite spectral dependence compared with the fundamental quasi-TE mode: it is anomalous for wavelength below 2354 nm but becomes normal for wavelength above. As a result, the phase-matching condition is quite different for this mode. It cannot be satisfied in the normal-dispersion regime above the ZDWL but can simultaneously support two modulational-instability sidebands when pumping in the anomalous-dispersion regime below 2354 nm [19, 21]. The theory presented in this section can be used to analyze the parametric process in this mode. However, as this mode has a much less mode confinement and tends to be cut off at a wavelength around 3.5 μm, the efficiency and tunability for parametric generation is limited. Therefore, we focus only on the fundamental quasi-TE mode in this paper.

3. Optical parametric oscillation

For a high-quality (high-Q) micro-resonator, the resonant modes participating in the nonlinear processes are nearly uniform along the cavity length, with a magnitude determined by the non-linear processes. It is thus more convenient to treat each resonant mode as an entity rather than looking into its detailed spatial distribution along the cavity. The pump and signal fields inside the cavity are found to satisfy the dynamic equations as (see Appendix):

$$\frac{dA_p}{dt} = i\Delta\omega_p A_p - \frac{A_p}{2\tau_{tp}} + \frac{i\omega_p \widetilde{n}_p^{f}}{n_{0p}} A_p + i\left(\gamma_p^c U_p + 2\gamma_{ps}^c U_s + 2\gamma_{pi}^c U_i\right) A_p + 2i\gamma_{pspi}^c A_s A_i A_p^* + \frac{iA_{in}}{\sqrt{\tau_{ep}}}, \tag{7}$$

$$\frac{dA_s}{dt} = i\Delta\omega_s A_s - \frac{A_s}{2\tau_{ts}} + \frac{i\omega_s \widetilde{n}_s^{f}}{n_{0s}} A_s + i\left(\gamma_s^c U_s + 2\gamma_{sp}^c U_p + 2\gamma_{si}^c U_i\right) A_s + i\gamma_{spip}^c A_p^2 A_i^*, \tag{8}$$

$$\frac{dA_i}{dt} = i\Delta\omega_i A_i - \frac{A_i}{2\tau_{ti}} + \frac{i\omega_i \widetilde{n}_i^{f}}{n_{0i}} A_i + i\left(\gamma_i^c U_i + 2\gamma_{ip}^c U_p + 2\gamma_{is}^c U_s\right) A_i + i\gamma_{ipsp}^c A_p^2 A_s^*, \tag{9}$$

where A_{in} and A_j ($j = p,s,i$) are slowly-varying field amplitudes of the input wave and the three waves inside the cavity, respectively. For convenience, we have normalized them such that $U_j = |A_j|^2$ represents the intracavity field energies but $|A_{in}|^2$ represents the input pump power. In Eqs. (7)-(9), the first term on the right side represents the frequency detuning $\Delta\omega_j = \omega_j - \omega_{0j}$ from the cavity resonance ω_{0j}. The second term governs the photon decay inside the cavity with a lifetime τ_{tj} of the loaded cavity. The third term describes the free-carrier effects where $\widetilde{n}_j^f = n_{fj} + ic\alpha_{fj}/(2\omega_j)$ and $n_{0j} = n_0(\omega_{0j})$ is the refractive index of silicon material at ω_{0j}. The final term of Eq. (7) represents the external power feeding for the pump wave, where τ_{ep} is the photon escape time associated with the external coupling.

The fourth and fifth terms of Eqs. (7)-(9) represents SPM, XPM, and FWM effects, with the cavity nonlinear parameters given by a form similar to Eq. (4) as

$$\gamma_{ijkl}^c = \frac{3\omega_i \eta_{ijkl}^c \chi^{(3)}(-\omega_i;\omega_j,-\omega_k,\omega_l)}{4\varepsilon_0 n_{0i} n_{0j} n_{0k} n_{0l} \bar{V}_{ijkl}}, \quad \text{with} \quad \eta_{ijkl}^c \equiv \frac{\int_{si} d\boldsymbol{r}(\varepsilon_{ri}\varepsilon_{rj}\varepsilon_{rk}\varepsilon_{rl})^{1/2}\widetilde{E}_i^*\widetilde{E}_j\widetilde{E}_k^*\widetilde{E}_l}{\left\{\prod_{v=i,j,k,l}\int_{si} d\boldsymbol{r}\varepsilon_{rv}^2|\widetilde{E}_v|^4\right\}^{1/4}}, \tag{10}$$

where $\bar{V}_{ijkl} \equiv (V_i V_j V_k V_l)^{1/4}$ is the *average* effective mode volume and V_v ($v = i,j,k,l$) is that at individual frequency ω_v given in Eq. (25) of Appendix. η_{ijkl}^c is the cavity mode overlap factor, where $\varepsilon_{rv} = \varepsilon_r(\boldsymbol{r},\omega_{0v})$ is the dielectric constant for the media, $\widetilde{E}_v = \widetilde{E}_v(\boldsymbol{r},\omega_{0v})$ is the electrical field for the cavity resonant mode at ω_{0v}, and the subscript si denotes the integral over the silicon core (see Appendix for details). In Eqs. (7)-(10), the superscript c denotes that the variables are cavity-related. Similar to the previous section, we also simplify the notations of SPM and XPM nonlinear parameters as $\gamma_v^c \equiv \gamma_{vvvv}^c$ and $\gamma_{uv}^c \equiv \gamma_{uvvu}^c$ for convenience.

Note that η_{ijkl}^c given in Eq. (10) describes the resonant mode overlap over the entire cavity. Therefore, apart from the transverse field overlap discussed in the previous section, the longitudinal mode overlap along the cavity affects significantly the FWM process. In particular, for an azimuthally symmetric resonator like a microdisk or microring, each resonance exhibits a unique angular momentum with a field distribution $\widetilde{E}_m(\boldsymbol{r},\omega_{0m}) \propto e^{im\phi}$ where m is an integer [22]. As a result, the requirement of longitudinal cavity-mode overlap imposes a selection rule for the FWM process, $2m_p = m_s + m_i$, where m_j ($j = p,s,i$) is the angular-momentum number for the three modes. In contrast to the linear momentum conservation for a straight waveguide described in the previous section, this selection rule regarding the phase-matching condition indicates the angular momentum conservation among the four interacting photons. Interestingly, for signal and idler modes copolarized with and symmetrically located around a pump mode, $m_{s/i} = m_p \pm l$ (l is an integer), the phase matching condition is automatically satisfied [23].
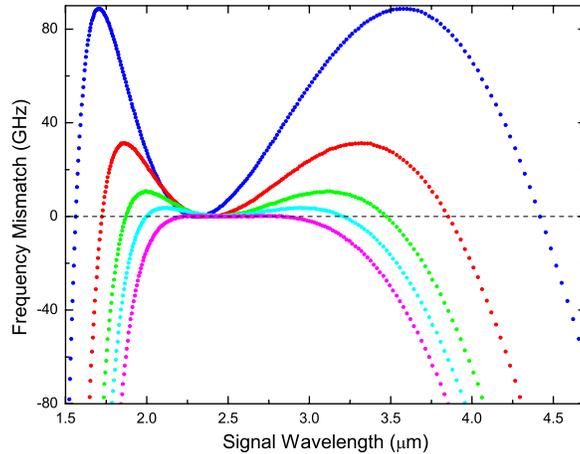
Fig. 4. Frequency mismatch of the resonant modes for a microring resonator with a diameter of 50.01 μm and a cross section of $1.7 \times 0.4\ \mu$m at various pump wavelengths. The frequency mismatch is defined as $(2\omega_{0p} - \omega_{0s} - \omega_{0i})/2\pi$ for angular-momentum conserved pump, signal, and idler $(2m_p = m_s + m_i)$. The pump mode is located at 2308.4 nm $(m_p = 195,$ blue), 2382.9 nm $(m_p = 187,$ red), 2431.9 nm $(m_p = 182,$ green), 2462.3 nm $(m_p = 179,$ cyan), and 2493.5 nm $(m_p = 176,$ pink), respectively. The resonant modes are simulated with the finite element method (FEMLAB, COMSOL).

Moreover, the energy conservation of $2\omega_p = \omega_s + \omega_i$ is also satisfied for the FWM process (see Appendix). However, due to the waveguide dispersion, this may not be so for the resonance frequencies, $2\omega_{0p} = \omega_{0s} + \omega_{0i}$, where the three waves are located. In this case, previous discussion about the phase matching condition in a straight waveguide can be applied to the microdisk or microring resonator, but in the frequency space rather than in the momentum space. As FWM becomes most efficient, because of cavity enhancement, when the three waves coincide with cavity resonances, it is essential to design the cavity appropriately such that the resonant frequencies can be matched at desired pump and signal/idler resonances. Figure 4 shows such an example of a microring resonator with a diameter of 50.01 μm and a cross section of $1.7 \times 0.4\ \mu$m, where the resonance frequency mismatch, $\Omega_0/2\pi \equiv (2\omega_{0p} - \omega_{0s} - \omega_{0i})/2\pi$, is plotted for angular-momentum conserved pump, signal, and idler $(2m_p = m_s + m_i)$. With a pump launched at the resonance of 2308.4 nm $(m_p = 195,$ blue), frequency matching can be satisfied for a signal mode at 1562.2 nm in the telecom band $(m_s = 318,$ corresponding idler mode at 4419.6 nm, $m_i = 72)$. Moreover, various frequency-matched signal resonance can be obtained by tuning the pump to appropriate cavity modes. For example, by tuning the pump wavelength to modes at 2382.9 nm $(m_p = 187,$ red), 2431.9 nm $(m_p = 182,$ green), and 2462.3 nm $(m_p = 179,$ cyan), frequency matching can be realized for signal resonances at 1724.4 nm $(m_s = 282)$, 1870.9 nm $(m_s = 255)$, and 1996.8 nm $(m_s = 235)$, respectively. When tuning the pump wavelength to the resonance at 2493.5 nm $(m_p = 176,$ pink) which is close to the ZDWL of the resonator, the frequency matching condition can be satisfied for a considerable number of signal modes over a broad band between 2230 and 2830 nm. Clearly, such a microring resonator enables highly tunable optical parametric oscillation. Equivalently, the tunable OPO can also be realized with a fixed pump wavelength, and changing the cavity geometry to shift the frequency-matched signal resonance.

Apart from the waveguide dispersion, Eqs. (7)-(9) show that SPM, XPM, and free-carrier dispersion all detune the cavity resonances and thus introduce frequency mismatches, which

are given by the following expressions:

$$\Omega_K \approx 2U_p \mathrm{Re}(\gamma_{sp}^c + \gamma_{ip}^{c*} - \gamma_p^c), \tag{11}$$

$$\Omega_f = \frac{\omega_s n_{fs}}{n_{0s}} + \frac{\omega_i n_{fi}}{n_{0i}} - 2\frac{\omega_p n_{fp}}{n_{0p}} \approx \omega_p^2 n_{fp}\left(\frac{1}{\omega_s n_{0s}} + \frac{1}{\omega_i n_{0i}} - \frac{2}{\omega_p n_{0p}}\right), \tag{12}$$

where the final approximation in Eq. (12) assumes a same cavity-averaged carrier density $\bar{N}$ experienced by the three waves ([2], see also Appendix). In Eq. (11), we have neglected SPM and XPM introduced by the signal and idler because they are in general much smaller than the pump. The total frequency mismatch for the FWM process is thus given by $\Omega = \Omega_0 + \Omega_K + \Omega_f$. Interestingly, free carrier and Kerr nonlinearity provide opposite contributions to the frequency mismatch, where Ω_K is generally positive but Ω_f is negative instead. For example, for a pump and signal at 2308.4 nm and 1562.2 nm, respectively, inside the ring resonator in Fig. 4, a pump energy of 1 pJ inside the resonator would introduce a frequency mismatch of $\Omega_K/2\pi = 0.74$ GHz. In contrast, a carrier density of 10^{15} cm^{-3} corresponds to a frequency mismatch of $\Omega_f/2\pi = -0.47$ GHz for the same set of pump, signal and idler. However, as our proposed OPO scheme dramatically reduces the creation of free carriers, the magnitude of Ω_f would be significantly smaller than Ω_K induced by SPM and XPM.

The power-dependent nonlinear frequency mismatch can be used to compensate the linear one introduced by waveguide dispersion. It broadens the bandwidth of parametric gain and thus reduces significantly the requirement for linear resonant-frequency matching. Such power-assisted frequency matching can be seen more clearly in Eqs. (7)-(9), which provide a parametric gain coefficient for a weak signal and idler given by

$$g^2 = \gamma_{spip}^c \gamma_{ipsp}^{c*} U_p^2 - (\Omega_0 + \Omega_K + \Omega_f + i\Delta)^2/4 \approx \gamma_{spip}^c \gamma_{ipsp}^{c*} U_p^2 - (\Omega_0 + \Omega_K)^2/4, \tag{13}$$

where Δ is the difference of total loss coefficients between the signal and idler. Clearly, a positive parametric gain can be obtained within a bandwidth of

$$-4U_p\sqrt{\gamma_{spip}^c \gamma_{ipsp}^{c*}} \approx -2U_p\sqrt{\gamma_{spip}^c \gamma_{ipsp}^{c*}} - \Omega_K < \Omega_0 < 2U_p\sqrt{\gamma_{spip}^c \gamma_{ipsp}^{c*}} - \Omega_K \approx 0. \tag{14}$$

This inequality shows clearly that the high incracavity pump energy enhanced by the high-Q factor significantly extends the bandwidth of resonant frequency matching required for parametric oscillation. As a rough estimate, for the resonator used in Fig. 4, 1-pJ pump energy inside the cavity provides a parametric bandwidth of around 1.5 GHz for the resonant-frequency matching. This value is more than two orders of magnitude larger than that available in silica microcavities for the same pump energy [23], thanks to the significantly higher Kerr nonlinearity of silicon. The pump energy of 1 pJ corresponds to an input power of only 0.4 mW at 2308.4 nm critically coupled into the ring resonator with a loaded Q factor of 10^6. As Eq. (10) shows that the magnitude of the nonlinear parameter is inversely proportional to the effective mode volume, the parametric bandwidth can be increased further by reducing the diameter of the resonator. Therefore, with such a power-enhanced frequency-matching condition, it should become readily possible to realize OPO with a relative small input power.

SOI ring resonators with Q as high as 10^6 have been demonstrated recently [24]. The photon lifetime is about 1 ns inside such a high-Q cavity, corresponding to an interaction length of ~ 8 cm for FWM, and thus provides efficient parametric generation. Moreover, a significant amount of pump energy is stored inside the cavity, leading to a dramatic reduction in the power requirement for lasing. The lasing threshold can be obtained from Eqs. (8) and (9) in the steady state when the parametric gain balances the cavity losses for both the signal and idler waves. Below the lasing threshold, the signal and idler are created only through parametric fluorescence. Their powers are so small that the SPM, XPM, and TPA are all dominated by the

pump wave. Moreover, free carriers are dominantly created through the self-TPA of the pump. Assume that the frequency matching condition is satisfied for the parametric process, Eqs. (8) and (9) provide the following general equation for the lasing threshold of the intracavity pump energy:

$$4\gamma_{\text{spip}}^{c}\gamma_{\text{ipsp}}^{c*}U_p^2 = (1/\tau_{\text{ts}} + c\alpha_{\text{fs}}/n_{0s} + 2\beta_{\text{Tsp}}^{c}U_p)(1/\tau_{\text{ti}} + c\alpha_{\text{fi}}/n_{0i} + 2\beta_{\text{Tip}}^{c}U_p), \qquad (15)$$

where $\beta_{\text{Tuv}}^{c} \equiv 2\text{Im}(\gamma_{\text{uv}}^{c})$ is the cavity-related cross-TPA coefficient. Consequently, by using Eq. (7), the lasing threshold for the input power is thus given by

$$P_{th} = \frac{\tau_{\text{ep}}}{4}U_p(1/\tau_{\text{tp}} + c\alpha_{\text{fp}}/n_{0p} + \beta_{\text{Tpp}}^{c}U_p)^2, \qquad (16)$$

where the threshold intracavity energy U_p is given by Eq. (15).

Equations (15) and (16) are quite general, as they includes all the effects of linear losses, TPA, and FCA. They can be used to find the lasing threshold for an arbitrary set of frequency-matched pump, signal, and idler. In particular, for our proposed scheme where the pump is located below the half band gap, the pump wave does not introduce self-TPA and free-carrier effects thus become negligible. Equations (15) and (16) then reduces to a simple form of the lasing threshold as

$$P_{th} = \frac{\tau_{\text{ep}}}{8\tau_{\text{tp}}^2} \frac{\rho_+ + \left[\rho_-^2 + \gamma_{\text{spip}}^{c}\gamma_{\text{ipsp}}^{c*}/(\tau_{\text{ts}}\tau_{\text{ti}})\right]^{1/2}}{\gamma_{\text{spip}}^{c}\gamma_{\text{ipsp}}^{c*} - \beta_{\text{Tsp}}^{c}\beta_{\text{Tip}}^{c}}, \qquad (17)$$

where $\rho_{\pm} \equiv (\beta_{\text{Tip}}^{c}/\tau_{\text{ts}} \pm \beta_{\text{Tsp}}^{c}/\tau_{\text{ti}})/2$. Equation (17) can be simplified further by noting that, for a pump located below the half band gap of silicon, the idler on the Stokes side does not experience cross-TPA and $\beta_{\text{Tip}}^{c} = 0$. In the absence of cross-TPA and nonlinearity dispersion, Eq. (17) reduces to the simple case like the silica microcavity [23]. As the photon lifetime is linearly dependent on the cavity Q factor, the lasing threshold is thus inversely proportional to the square of the cavity Q factor [23], since the cavity resonance increases both the FWM interaction length and the stored pump energy. Cross-TPA increases cavity losses and thus increases the lasing threshold.

Figure 5 shows the lasing threshold at various signal wavelengths inside the microring resonator used in Fig. 4. The resonator is assumed to have a moderate intrinsic Q factor of 5×10^5. As discussed previously, the lasing wavelength can be tuned by changing either the pump wavelength or the resonator geometry. As an example to illustrate the underlying physics with simplicity, we fix the pump wavelength at 2308.4 nm so that a signal can lase in the telecom band (red spots). For simplicity, we also assume a critical coupling at all three waves [25] and a perfect frequency matching for various signal wavelengths. Because of the ring geometry, both the effective mode volume and the mode overlap factor become more dispersive than the straight waveguide. For example, the effective mode volume changes from 55 μm^3 at a telecom wavelength of 1.5 μm to 72 μm^3 at the pump wavelength, and further nearly doubles to 141 μm^3 at a mid infrared wavelength of 5.0 μm. On the other hand, the mode overlap factor $|\eta_{\text{spip}}|$ changes from 1 to 0.90 when the signal is tuned from the pump wavelength to telecom band at 1.5 μm. However, detailed analysis shows that these dispersive effects only slightly affect the efficiency of parametric oscillation, and significantly enhanced FWM inside the cavity enables a relatively low lasing threshold.

Figure 5 shows that, for a lasing wavelength between 2.103 and 2.559 μm, the sum energy of the pump and signal/idler photons falls below the half band gap, and OPO is completely free from both TPA and FCA, resulting in a low lasing threshold of about 1.68 mW. When the lasing wavelength moves outside this spectral region, cross-TPA starts to effect, which increases the lasing threshold. Even so, the lasing threshold is still as low as about 2.24 mW at a telecom
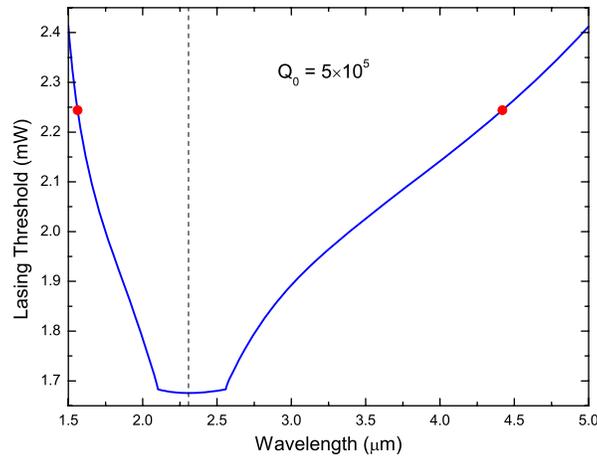
Fig. 5. OPO lasing threshold for the micro-ring resonator used in Fig. 4. The pump wavelength is fixed at 2308.4 nm (dashed line) and critical coupling is assumed at all three waves. The red spot shows the frequency-matched signal and idler modes at 1562.2 and 4419.6 nm, respectively (see Fig. 4). Note that the two kinks at 2103 and 2559 nm are numerical artifacts because of the kink in TPA coefficient at 2.2 μm (see Ref. [16]). In practice, the lasing threshold would change smoothly with signal wavelength.

wavelength of 1.562 μm. Clearly, CW parametric oscillation is readily available over a broad band just with a mW-level pump power. The lasing threshold can be further reduced by using a smaller resonator, since the efficiency of FWM is inversely proportional to the effective mode volume of the cavity [see Eqs. (10) and (17)]. Moreover, although the numerical example shown in Fig. 5 assumes a critical coupling at both signal and idler, Eq. (17) shows that the lasing threshold can be further reduced by reducing the external coupling of one wave to increase its loaded photon lifetime. In particular, most practical situations concern the output of only one wave (say, the signal), and we can reduce the lasing threshold by letting the idler only circulate inside the cavity. This is quite easy to realize in practice, since the bus waveguide used for the external coupling generally has a limited coupling bandwidth and it is hard to maintain critical coupling at both widely separated signal and idler wavelengths, unless some specific technique is used [25].

Note that silicon has a Raman scattering coefficient much larger than Kerr nonlinearity. For an azimuthally symmetric microring resonator on a (1 0 0) wafer, Raman scattering is allowed for the quasi-TE modes to transfer its energy to a quasi-TM mode at a frequency 15.6 THz away (or to another quasi-TE mode but with an azimuthally varying Raman gain coefficient). As a result, the threshold of Raman lasing would be lower than that of OPO. If possible, Raman scattering would start to lase first, which would quench optical parametric oscillation. However, thanks to the narrow bandwidth of Raman scattering in silicon, Raman lasing can be prohibited simply by choosing the resonator radius such that Raman Stokes wave is detuned from the cavity resonances. This is the case of the microring resonator used in Figs. 4 and 5, where the Raman Stokes wave 15.6 THz away from the 2308.4-nm pump does not coincide with any quasi-TM or TE resonance. Same do other pump modes used in Fig. 4. Therefore, silicon-based OPO does not suffer from the lasing competition between FWM and stimulated Raman scattering [23], which severely limits the operation regime for OPO inside silica microcavities.

4. Conclusion

In conclusion, we have proposed a novel scheme for CW optical parametric oscillation inside silicon micro-resonators. This scheme is not only free from the commonly encountered FCA obstacle, but also exhibits an extremely large tunability by simply tuning the pump wavelength or changing the waveguide geometry. We have shown that, with a moderate Q factor of the resonator, lasing with a relatively low threshold is available over an extremely broad spectrum extending from the telecom band to the mid infrared. Various kinds of lasers [26], *i.e.*, antimonide quantum-well laser diodes or Tm-doped fiber lasers, can be used as a pump for this purpose. Currently, significant efforts have been made to develop mid-infrared light sources because of the broad potential applications from free-space communication, trace-gas sensing, high-resolution molecular spectroscopy, to medical diagnostics and surgery [26]. Although silicon Raman laser was proposed and demonstrated recently for this purpose [27–29], its lasing frequency is primarily fixed with respect to the pump. In contrast, our proposed CW OPO can provide a much larger bandwidth and broader tunability, comparable with those available in $\chi^{(2)}$ materials like periodically-poled $LiNbO_3$ waveguide. By using the significant Kerr nonlinearity inside high-quality silicon micro-resonators, we expect that our proposed silicon-based CW OPO would provide an efficient solution for the broad applications in both the telecom band and mid infrared, and thus help extend nonlinear silicon photonics into a new spectral regime.

5. Appendix

Here we provide the derivation of Eqs. (7)-(9) governing the parametric oscillation inside a silicon micro-resonator. In general, an optical field inside a micro-cavity satisfies the wave equation in the frequency domain as

$$\nabla^2 \widetilde{\boldsymbol{E}}(\boldsymbol{r},\omega) + \frac{\omega^2}{c^2}\varepsilon_r(\boldsymbol{r},\omega)\widetilde{\boldsymbol{E}}(\boldsymbol{r},\omega) = -\mu_0\omega^2\widetilde{\boldsymbol{P}}(\boldsymbol{r},\omega), \tag{18}$$

where ε_r is the dielectric constant of the media, $\widetilde{\boldsymbol{P}} = \widetilde{\boldsymbol{P}}^{\mathrm{f}} + \widetilde{\boldsymbol{P}}^{(3)}$ where $\widetilde{\boldsymbol{P}}^{\mathrm{f}}$ and $\widetilde{\boldsymbol{P}}^{(3)}$ are free-carrier-induced polarization and third-order nonlinear polarization, respectively.

In the absence of free-carrier and nonlinear effect, Eq. (18) for a microcavity with a specific geometry leads to a series of resonant eigenmodes $\widetilde{\boldsymbol{E}}_j(\boldsymbol{r},\omega_{0\mathrm{j}})$ at the discrete resonant frequencies $\omega_{0\mathrm{j}}$. As the carrier and nonlinear effects are only small perturbations to the dominant linear wave evolution, the optical field in the presence of carrier and nonlinear effects can be written in the base of the unperturbed resonant eigenmodes as

$$\widetilde{\boldsymbol{E}}(\boldsymbol{r},\omega) = \sum_j \widetilde{A}_j(\omega)\widetilde{\boldsymbol{E}}_j(\boldsymbol{r},\omega_{0\mathrm{j}}). \tag{19}$$

Substituting Eq. (19) into Eq. (18), multiplying it with the resonant field of $\widetilde{\boldsymbol{E}}_i(\boldsymbol{r},\omega_{0\mathrm{i}})$, integrating over the entire cavity, applying the mode orthogonality, and transforming the resulting equation into the time domain, we obtain the following dynamic equation:

$$\frac{d^2A_i}{dt^2} + \omega_{0\mathrm{i}}^2 A_i = -\frac{\frac{d^2}{dt^2}\int d\boldsymbol{r}\widetilde{\boldsymbol{E}}_i^*(\boldsymbol{r},\omega_{0\mathrm{i}})\cdot\boldsymbol{P}(\boldsymbol{r},t)}{\varepsilon_0\int d\boldsymbol{r}\varepsilon_r(\boldsymbol{r},\omega_{0\mathrm{i}})|\widetilde{\boldsymbol{E}}_i(\boldsymbol{r},\omega_{0\mathrm{i}})|^2}. \tag{20}$$

Assume the optical field is around a carrier frequency ω_i which is nearby a cavity resonance $\omega_{0\mathrm{i}}$, and with a bandwidth much smaller than the free-spectral range of the cavity. We can write the field amplitude and polarization as $A_i(t) = A_i'(t)e^{-i\omega_i t}$ and $\boldsymbol{P}(\boldsymbol{r},t) = \boldsymbol{P}'(\boldsymbol{r},t)e^{-i\omega_i t}$, where A_i' and $\boldsymbol{P}'$ are both slowly-varying amplitudes. Substituting these two expressions into Eq. (20)

and leaving terms only up to the first order, we obtain the following equation governing the slowly-varying field amplitude as

$$\frac{dA_i}{dt} = i(\omega_i - \omega_{0i})A_i - \frac{A_i}{\tau_{ti}} + \frac{i\omega_i}{2\varepsilon_0} \frac{\int d\boldsymbol{r} \widetilde{\boldsymbol{E}}_i^*(\boldsymbol{r}, \omega_{0i}) \cdot \boldsymbol{P}(\boldsymbol{r}, t)}{\int d\boldsymbol{r} \varepsilon_r(\boldsymbol{r}, \omega_{0i})|\widetilde{\boldsymbol{E}}_i(\boldsymbol{r}, \omega_{0i})|^2},$$ (21)

where we have dropped the prime notation for simplicity. In Eq. (21), we have counted in the linear losses of the cavity, indicating by the photon lifetime τ_{ti} of the loaded cavity for the resonance at ω_{0i}. It is related to the cavity Q factor as $\tau_{ti} = Q_{ti}/\omega_{0i}$.

Silicon micro-resonators generally exhibit a significant birefringence. In general, the resonance frequencies of quasi-TE modes do not coincide with those of quasi-TM modes, resulting in a high polarization purity of cavity resonances. Because of the birefringence, momentum conservation required for the FWM process (see the main text) causes FWM to occur most commonly among waves with a same polarization. These considerations allow us to focus in the following on a specific scalar case where all the optical fields are linearly copolarized with each other. The derivations can be easily extended to the more general vector case. As nonlinear wave interactions inside a microcavity typically involves only a few optical waves, each with a limited bandwidth around a cavity resonance, the free-carrier-induced polarization and the third-order nonlinear polarization are then given by [2]

$$P^f(\boldsymbol{r}, t) = \varepsilon_0 \sum_j \chi^f[\omega_j, N(\boldsymbol{r}, t)]A_j(t)e^{-i\omega_j t}\widetilde{E}_j(\boldsymbol{r}, \omega_{0j}),$$ (22)

$$P^{(3)}(\boldsymbol{r}, t) = \frac{3}{4}\varepsilon_0 \sum_{jkl} \chi^{(3)}_{ijkl}A_j(t)A_k^*(t)A_l(t)e^{-i(\omega_j - \omega_k + \omega_l)t}\widetilde{E}_j(\boldsymbol{r}, \omega_{0j})\widetilde{E}_k^*(\boldsymbol{r}, \omega_{0k})\widetilde{E}_l(\boldsymbol{r}, \omega_{0l}),$$ (23)

where χ^f is the carrier-induced susceptibility which is related to the carrier-induced refractive index change and absorption [2] as $\chi^f(\omega, N) = 2n_0(\omega)[n_f(\omega, N) + ic\alpha_f(\omega, N)/(2\omega)]$, where n_f and α_f is given in the text by the Drude model. In Eq. (23), $\chi^{(3)}_{ijkl} \equiv \chi^{(3)}(-\omega_i; \omega_j, -\omega_k, \omega_l)$ is the third-order nonlinear susceptibility. Clearly, the third-order nonlinear process creates frequency components with $\omega_i = \omega_j + \omega_l - \omega_k$, which indicates the energy conservation among the four interacting photons. By noting that both the carrier and nonlinear effects are dominantly contributed from the silicon core and χ^f is nearly linearly dependent on the carrier density, substituting into Eq. (21) the slowly-varying polarization amplitudes of Eqs. (22) and (23) at individual frequency ω_i, we arrive at the final dynamic equation governing the field amplitude as

$$\frac{dA_i}{dt} = i(\omega_i - \omega_{0i})A_i - \frac{A_i}{\tau_{ti}} + \frac{i\omega_i}{2n_{0i}^2}\chi^f(\omega_i, \bar{N}_i)A_i + i\sum_{jkl} \gamma^c_{ijkl}A_jA_k^*A_l,$$ (24)

where $n_{0i} = n_0(\omega_{0i})$ is the material refractive index of silicon at ω_{0i}, and the field amplitudes have been normalized such that $U_v = |A_v|^2$ represents the field energy of mode v inside the cavity. In Eq. (24), we have used the photon energy conservation $\omega_i + \omega_k = \omega_j + \omega_l$ for the third-order nonlinear term. The nonlinear parameter γ^c_{ijkl} is given by Eq. (10), with an effective mode volume V_v at individual frequency ω_v given by

$$V_v \equiv \frac{\left\{\int d\boldsymbol{r}\varepsilon_r(\boldsymbol{r}, \omega_{0v})|\widetilde{E}_v(\boldsymbol{r}, \omega_{0v})|^2\right\}^2}{\int_{si} d\boldsymbol{r}\varepsilon_r^2(\boldsymbol{r}, \omega_{0v})|\widetilde{E}_v(\boldsymbol{r}, \omega_{0v})|^4},$$ (25)

where the subscript si in the integral denotes the integral over the silicon core.

In Eq. (24), $\bar{N}_i$ is the cavity-averaged carrier density given by

$$\bar{N}_i(t) \equiv \frac{\int_{si} d\mathbf{r} N(\mathbf{r},t)\varepsilon_r(\mathbf{r},\omega_{0i})|\widetilde{E}_i(\mathbf{r},\omega_{0i})|^2}{\int d\mathbf{r}\varepsilon_r(\mathbf{r},\omega_{0i})|\widetilde{E}_i(\mathbf{r},\omega_{0i})|^2}. \tag{26}$$

As a result, different resonant modes may experience different free-carrier effects even for a same carrier distribution, if their mode profiles overlap with the carrier distribution quite differently. The cavity-averaged carrier density satisfies a simple equation as [2]

$$\frac{d\bar{N}_i}{dt} = \bar{G}_i - \frac{\bar{N}_i}{\tau_0}, \qquad \text{with} \quad \bar{G}_i(t) \equiv \frac{\int_{si} d\mathbf{r} G(\mathbf{r},t)\varepsilon_r(\mathbf{r},\omega_{0i})|\widetilde{E}_i(\mathbf{r},\omega_{0i})|^2}{\int d\mathbf{r}\varepsilon_r(\mathbf{r},\omega_{0i})|\widetilde{E}_i(\mathbf{r},\omega_{0i})|^2}, \tag{27}$$

where τ_0 is the effective carrier lifetime, $\bar{G}_i$ is the cavity-averaged carrier generation rate, and $G(\mathbf{r},t)$ is the local carrier-generation rate at the spatial location $\mathbf{r}$. For the optical parametric processes considered here, the free carriers are created through TPA and $G(\mathbf{r},t)$ can thus be obtained from the TPA-induced optical energy dissipation.

Equation (23) shows that the SPM, XPM, and TPA related nonlinear polarization at the carrier frequency ω_u is given by

$$P_u^{(3)}(\mathbf{r},t) = \frac{3\varepsilon_0}{4} e^{-i\omega_u t} A_u(t)\widetilde{E}_u \left\{ \chi_{\text{uuuu}}^{(3)}|A_u(t)|^2|\widetilde{E}_u|^2 + 2\sum_{v,v\neq u} \chi_{\text{uvvu}}^{(3)}|A_v(t)|^2|\widetilde{E}_v|^2 \right\}, \tag{28}$$

where $\widetilde{E}_v$ stands for $\widetilde{E}_v(\mathbf{r},\omega_{0v})$. Therefore, TPA-induced energy dissipation rate is the sum of that for the individual waves at ω_u, which has the following form of

$$\sum_u \left\{ \frac{1}{4} E_u^*(\mathbf{r},t) \frac{\partial P_u^{(3)}(\mathbf{r},t)}{\partial t} + c.c \right\}$$

$$= \frac{3\varepsilon_0}{8} \left\{ \sum_u \omega_u \text{Im}(\chi_{\text{uuuu}}^{(3)})|A_u|^4|\widetilde{E}_u|^4 + \sum_{u,v,v\neq u} (\omega_u + \omega_v)\text{Im}(\chi_{\text{uvvu}}^{(3)})|A_u|^2|A_v|^2|\widetilde{E}_u|^2|\widetilde{E}_v|^2 \right\}, \tag{29}$$

where $E_u(\mathbf{r},t) \equiv A_u(t)\widetilde{E}_u(\mathbf{r},\omega_{0u})e^{-i\omega_u t}$ on the left side stands for the time-dependent electric field component at ω_u, and $c.c$ denotes complex conjugate. It is easy to recognize from Eq. (29) that its first and second terms describe the self- and cross-TPA, respectively. Therefore, the local carrier generation rate is thus given by

$$G(\mathbf{r},t) = \frac{3\varepsilon_0}{8\hbar} \left\{ \frac{1}{2}\sum_u \text{Im}(\chi_{\text{uuuu}}^{(3)})|A_u|^4|\widetilde{E}_u|^4 + \sum_{u,v,v\neq u} \text{Im}(\chi_{\text{uvvu}}^{(3)})|A_u|^2|A_v|^2|\widetilde{E}_u|^2|\widetilde{E}_v|^2 \right\}. \tag{30}$$

Substituting this expression into Eq. (27), we find the cavity-averaged carrier-generation rate given by the following expression

$$\bar{G}_i(t) = \sum_u \frac{c^2\beta_{\text{Tuu}}\eta_{\text{iuu}}^{\text{f}}U_u^2}{2\hbar\omega_u n_{0u}^2(\bar{V}_{\text{iuu}}^{\text{f}})^2} + \sum_{u,v,u\neq v} \frac{c^2\beta_{\text{Tuv}}\eta_{\text{iuv}}^{\text{f}}U_uU_v}{\hbar\omega_u n_{0u}n_{0v}(\bar{V}_{\text{iuv}}^{\text{f}})^2}, \tag{31}$$

where β_{Tvv} and β_{Tuv} are the conventionally defined coefficients for self- and cross-TPA [2], respectively, given by $\beta_{\text{Tuv}} \equiv 3\omega_u\text{Im}(\chi_{\text{uvvu}})/(2\varepsilon_0 c^2 n_{0u}n_{0v})$. $\bar{V}_{\text{iuv}}^{\text{f}} = (V_i^{\text{f}}V_u^{\text{f}}V_v^{\text{f}})^{1/3}$ is the *average* effective mode volume related to TPA-induced free-carrier effect, where V_v^{f} is the free-carrier related mode volume given by [30]

$$V_v^{\text{f}} \equiv \left\{ \frac{\left[\int d\mathbf{r}\varepsilon_r(\mathbf{r},\omega_{0v})|\widetilde{E}_v(\mathbf{r},\omega_{0v})|^2 \right]^3}{\int_{si} d\mathbf{r}\varepsilon_r^3(\mathbf{r},\omega_{0v})|\widetilde{E}_v(\mathbf{r},\omega_{0v})|^6} \right\}^{1/2}, \tag{32}$$

and $\eta_{\text{iuv}}^{\text{f}}$ is the cavity-mode overlap factor related to the TPA-induced carrier effects, given by

$$\eta_{\text{iuv}}^{\text{f}} \equiv \frac{\int_{si} d\boldsymbol{r} \varepsilon_{ri} \varepsilon_{ru} \varepsilon_{rv} |\widetilde{E}_i|^2 |\widetilde{E}_u|^2 |\widetilde{E}_v|^2}{\left\{ \prod_{j=i,u,v} \int_{si} d\boldsymbol{r} \varepsilon_{rj}^3 |\widetilde{E}_j|^6 \right\}^{1/3}}. \tag{33}$$

Equations (24), (27), and (31) are quite general and can be used to describe various third-order nonlinear dynamics inside a microcavity. For the optical parametric process discussed in this paper, the optical wave consists of three waves locating around three different resonances. Substituting the three field amplitudes into Eqs. (24) and (31), decomposing them into equations for individual modes, and counting in the external power feeding for the pump wave, we obtain Eqs. (7)-(9).

Acknowledgment